

# Towards classification of experimental Laguerre–Gaussian modes using convolutional neural networks

Safura Sharifi,<sup>a,b,c,\*</sup>† Yaser Banadaki,<sup>c,d,†</sup> Georgios Veronis,<sup>a,b</sup> and Jonathan P. Dowling<sup>c,‡</sup>

<sup>a</sup>Louisiana State University, School of Electrical Engineering and Computer Science, Baton Rouge, Louisiana, United States

<sup>b</sup>Louisiana State University, Center for Computation and Technology, Baton Rouge, Louisiana, United States

<sup>c</sup>Louisiana State University, Hearne Institute for Theoretical Physics, Department of Physics and Astronomy, Baton Rouge, Louisiana, United States

<sup>d</sup>Southern University and A&M College, Department of Computer Science, Baton Rouge, Louisiana, United States

**Abstract.** Automated detection of orbital angular momentum (OAM) can tremendously contribute to quantum optical experiments. We develop convolutional neural networks to identify and classify noisy images of Laguerre–Gaussian (LG) modes collected from two different experimental set ups. We investigate the classification performance measures of the predictive classification models for experimental conditions. The results demonstrate accuracy and specificity above 90% in classifying 16 LG modes for both experimental set ups. However, the *F*-score, sensitivity, and precision of the classification range from 57% to 92%, depending on the number of imperfections in the images obtained from the experiments. This research could enhance the application of OAM light in telecommunications, sensing, and high-resolution imaging systems. © 2020 Society of Photo-Optical Instrumentation Engineers (SPIE) [DOI: [10.1117/1.OE.59.7.076113](https://doi.org/10.1117/1.OE.59.7.076113)]

**Keywords:** convolutional neural networks; orbital angular momentum; quantum optical experiments.

Paper 20200422 received Apr. 14, 2020; accepted for publication Jul. 14, 2020; published online Jul. 22, 2020.

## 1 Introduction

Orbital angular momentum (OAM)<sup>1,2</sup> arises from the helical phase front of a light beam. It is the component of angular momentum of the light beam that depends on the spatial field distribution and not on the polarization. The use of an OAM beams allows the development of improved sensing and imaging technologies, such as increased information transfer rate and data transmission capacity in optical communications,<sup>3</sup> automated microscopic detector arrays in high-resolution biological imaging systems,<sup>4</sup> improved photon detection in extended astronomical objects,<sup>5</sup> and increased alphabets in quantum cryptography.<sup>6</sup>

The helical phase structure of light results in the light possessing quantized values of OAM.<sup>7</sup> Examples of paraxial beams that possess OAM include Laguerre–Gaussian (LG),<sup>8</sup> Hermite–Gaussian,<sup>9</sup> Bessel–Gaussian,<sup>10</sup> Mathieu–Gaussian,<sup>11</sup> and Ince–Gaussian<sup>12</sup> beams. LG modes are the higher-order solutions to the paraxial wave equation in cylindrical coordinates with circular symmetry.<sup>13</sup> They are directly related to the quantized OAM of photons<sup>14,15</sup> resulting in various applications for OAM transfer, such as in light–matter interactions.<sup>16,17</sup> However, the coherent detection of LG modes generated by spatial light modulators (SLMs) is challenging. These modes are prone to mode loss and mode crosstalk<sup>13,18</sup> and contain imperfections due to

---

\*Address all correspondence to Safura Sharifi, E-mail: [sshari2@lsu.edu](mailto:sshari2@lsu.edu)

†These authors contributed equally to this paper.

‡Deceased 5 June 2020.

various sources of noise (i.e., turbulence) that mix information between adjacent modes and degrade the optical signal.<sup>19,20</sup>

To classify OAM modes, conventional sorting methods such as conjugate-mode sorters and scale factors are typically used. However, these methods require a complicated optical alignment process because the presence of turbulence causes the mixing of information between adjacent modes, which makes these techniques inaccurate.<sup>21</sup> For instance, the high sensitivity of OAM light to atmospheric turbulence<sup>13</sup> makes error-free OAM mode detection in free-space communications challenging, particularly when a large number of OAM modes are used.<sup>22,23</sup> The identification of the mode information for signals that carry more than a specific amount of noise using the centroid and radius of the beam profile captured by a CCD or CMOS camera<sup>24</sup> is challenging. As such, it is crucial to have an accurate method to classify the OAM beam detected at the receiving end of an optical communication platform.

Machine learning (ML) has a transformative impact on many underlying fields of basic research.<sup>25,26</sup> It is beginning to play an important role in automated analysis and adaptive control of atomic, molecular, and optical experiments. Recently, convolutional neural networks (CNNs)<sup>27</sup> and the transfer learning approach<sup>28</sup> have been shown to remarkably improve automated image interpretation with near-human accuracy.<sup>29,30</sup> ML techniques have been applied to the related task of detecting the OAM mode<sup>1,21,31</sup> with accuracies far better than those of the conjugate-mode sorting method.<sup>3</sup> Krenn et al.<sup>32</sup> used an artificial neural network (ANN) to distinguish between the transmitted OAM modes of light that have significant distortions after transmission over a distance of 143 km. Lohani et al.<sup>1</sup> demonstrated the ability of deep neural networks to classify LG modes when the training and test datasets are generated using computer simulations. However, the strength of the model needs to be evaluated for generalizing and adapting to different experimental conditions when the amount of noise varies depending on the optical arrangements. The influence of strong noise sources can cause offset in the background counts and even saturate the camera. This makes the identification of OAM modes using conventional denoising and averaging techniques seriously restricted in both speed and accuracy.<sup>33</sup> In free-space optical communication systems, the OAM shift-keying techniques require high-speed OAM identification methods. One of the main benefits of CNN-based techniques is that, after training, the mode recognition and classification can be applied extremely quickly. It has been demonstrated<sup>34</sup> that CNN-based OAM mode identification methods have a certain antiturbulence immunity leading to a high recognition accuracy and fast recognition time compared to other mode recognition techniques using aperture diffraction<sup>35,36</sup> and cylindrical lens detection methods.<sup>37,38</sup>

Doster and Watnik<sup>21</sup> used the Alexnet architecture for the CNN model to demultiplex the OAM-carrying beams by capturing an image of the unique multiplexing intensity pattern with the simulated atmospheric turbulence in a laboratory setting. However, pretrained models, such as GoogLeNet (Inception),<sup>39</sup> reduce the number of computations and storage costs for the network weights and have proven to outperform the classification accuracy obtained by the Alexnet architecture. Hofer et al.<sup>9</sup> used CNN to classify the 21 lowest unique Hermite Gaussian modes of a laser beam with an accuracy of 99%, whose experimental dataset was acquired from one optical set up utilizing an SLM. In addition to high accuracy, a sound classifier must also demonstrate high performance for other measures such as specificity, *F*-score, sensitivity, and precision.

In this paper, we examine the ability of CNN models to automatically classify the experimental images of LG modes based only on the intensity profile of their unique patterns in the presence of noise and imperfections in two experimental set ups. The use of the intensity profile of the detected modes allows for considerable simplification of current measurement schemes and results in lower error rates than the scale factor techniques. A large number of labeled simulated datasets was generated, and different amounts of noise are added to the simulated datasets to replicate imperfections of real experimental conditions. The testing data used to examine the ability of the zero-shot learning approach are real experimental images, while the CNN model is solely trained with instances of simulated data. This study may enable new applications of OAM light in telecommunications and high-resolution imaging systems.

The rest of the paper is organized as follows: Sec. 2 presents the two experimental arrangements and the theoretical framework of LG modes that are used to collect the training and testing datasets. Section 3 discusses the procedure for training and optimizing the performance of the

CNN model. In Sec. 4, the results for automated identification of LG modes are presented to assess the strengths and limits of the CNN model in generalizing and adapting to experimental conditions by studying the five performance measures of the classification. Section 5 discusses the advantages and performance of the CNNs in recognizing OAM modes, as well as potential applications. Finally, our conclusions are summarized in Sec. 6.

## 2 Data Collection for Training Data-Driven Predictive Model

### 2.1 Generating Experimental Datasets of OAM Modes

The experimental data are generated using two experimental set ups with different noise intensity, spatial dislocation, and nonuniform intensity in LG modes to examine the performance of the CNN model in generalizing to different experimental conditions. Figure 1(a) shows the first experimental set up that generates LG modes. A laser beam with a wavelength of 633 nm is coupled to a single-mode fiber (SMF) before being collimated with a 5-cm lens, which helps us to clean the beam to a Gaussian beam. The collimated Gaussian beam hits the SLM where the desired LG modes are encoded holographically.<sup>40</sup> The SLM is programmable, and the projected light to the mask or hologram can be controlled through a computer program. The reflected beam from the SLM contains many diffraction orders. The parameters are set to make the first diffraction order bright enough for the experiment. An iris placed at the Fourier plane acts as a filter to select the desired diffraction order. The beam profile thus selected is collimated with the final 25-cm lens. A CCD camera at the image plane records the intensity profiles of the desired LG modes.<sup>31,41</sup>

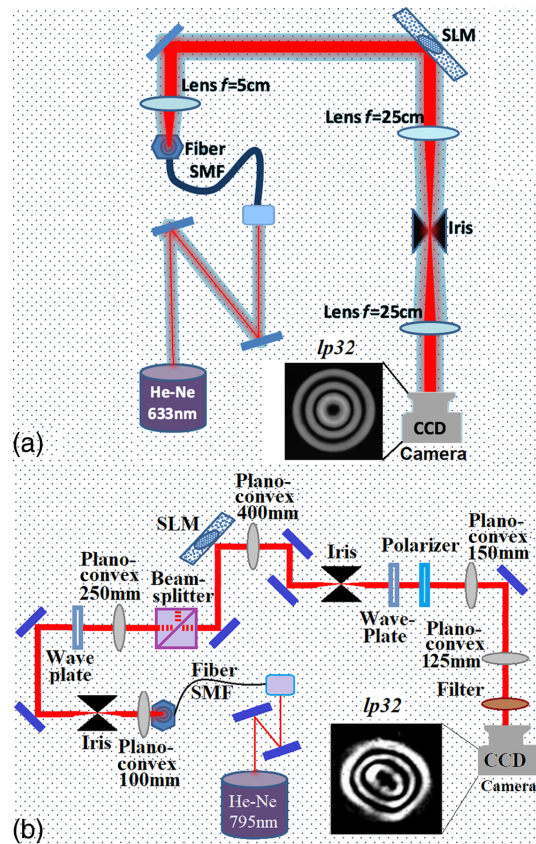


**Fig. 1** Experimental arrangements for the (a) first and (b) second quantum optical systems for generating arbitrary LG beams.<sup>20</sup> The CCD camera has a dynamic range of 82 dB with 60 ke-ll well capacity, median read noise of 3.6 e- rms, and peak counts of 200 per 500 ms.

The second experimental set up for LG modes' generation is shown in Fig. 1(b). Light from a 795-nm laser is coupled into an SMF and propagated through a telescope formed by two lenses to increase the size of the laser beam and illuminate as much SLM area as possible. The beam is passed through an iris for additional mode cleaning. The wave plate and polarization beam splitter combo are then used to control the light power to make sure that the camera is not saturated. The edge mirror reflects the beam to the SLM, then a regular mirror picks up the reflected beam. The combination of three lenses after the SLM focuses the beam at the iris that cleans up any higher diffraction orders, shrinks the beam back to small size, and focuses it on the camera. In the second experimental set up, light travels through more optical elements and lenses. This leads to more spatial dislocation and nonuniform intensity in the LG modes compared to the first experimental set up. This may also cause the slight ellipticity in the observed intensity patterns that could possibly be attributed to the presence of other, weaker optical modes,<sup>42</sup> or to the perturbation caused by the imperfect alignment of components<sup>43</sup> in the second experiment. The labeled experimental datasets of the LG modes are generated for testing CNN models using the set ups of an SLM and beam profiler.<sup>31</sup>

## 2.2 Generating Theoretical Datasets of OAM Modes

The LG modes are represented by the theoretical expression<sup>44</sup>

$$\begin{aligned}
 u_{l,p}(r, \phi, z) = & \frac{C_{lp}^{LG}}{w(z)} \left[ \frac{r\sqrt{2}}{w(z)} \right]^{|l|} \exp \left[ -\frac{r^2}{w^2(z)} \right] \\
 & L_p^{|l|} \left[ \frac{2r^2}{w^2(z)} \right] \exp \left[ -ik \frac{r^2}{2R(z)} \right] \exp(-ikz) \\
 & \exp(il\phi) \exp[i(2p + |l| + 1)\zeta(z)], \tag{1}
 \end{aligned}$$

where  $r$ ,  $\phi$ , and  $z$  are the cylindrical coordinates;  $l$  and  $p$  are the azimuthal and radial indices, which are integers;  $p > 0$ ;  $C_{lp}^{LG} = \sqrt{2p!/\pi(|l|+p)!}$  is a normalization constant;  $L_p^{|l|}$  is the associated Laguerre polynomial;  $\lambda$  is the wavelength;  $k = 2\pi/\lambda$  is the wavenumber;  $w(z) = w_0\sqrt{1 + (z/z_R)^2}$  is the beam waist;  $w_0$  is the beam waist at the beam focus;  $z_R = \pi w_0^2/\lambda$  is the Rayleigh range;  $R(z) = z[1 + (z/z_R)^2]$  is the radius of curvature; and  $\zeta(z) = \arctan(z/z_R)$  is the Gouy phase. Equation (1) is used to generate a theoretical image dataset of the first 16 LG modes ( $l$  and  $p$  vary from 0 to 3) for training the CNN model.

In order to replicate imperfections of real experimental conditions, substantial amounts of experimental data are generated and analyzed to estimate the approximate amplitude of the noise. Gaussian noise, Poisson noise, speckle noise, and camera blur in the first and second experiments are added to the simulated images in MATLAB<sup>®</sup>. In an optical communication channel, the intensity noise or modal noise is separated into additive noise and multiplicative noise.<sup>45</sup> The unwanted signal modifications at the input and output of an optical communications channel are modeled by random additive Gaussian noise. The effects of scattering and absorption on the signal transmitted in an optical communications channel are modeled by speckle and Poisson noises as random multiplicative noise sources.<sup>1,45</sup>

In order to extract the best standard deviation of the Gaussian and speckle noises and replicate real noise values seen on the sensors of the first and second experiments, CNN models are trained by generating the train datasets. These consist of the simulated images of an LG mode with a standard deviation in each class. The experimental images of the same LG mode are tested, as shown in Fig. 2. It can be observed in Fig. 2(a) that the average confidence of the classification for Gaussian noise is maximized around the standard deviation of  $\sigma = 0.04$  to 0.045 for the second experiment, while the standard deviation estimated by the CNN model for the first experiment is smaller than  $\sigma = 0.005$ . Figure 2(b) shows the estimated standard deviations of speckle noise that inherently exists in and degrades the quality of the optical images. The standard deviation of speckle noise is estimated to be smaller than  $\sigma = 0.04$  for the first experiment with the maximum confidence in the range of  $\sigma = [0.02, 0.03]$ , while the standard deviation of the second experiment is found to be in the range of  $\sigma = [0.08, 0.12]$ .

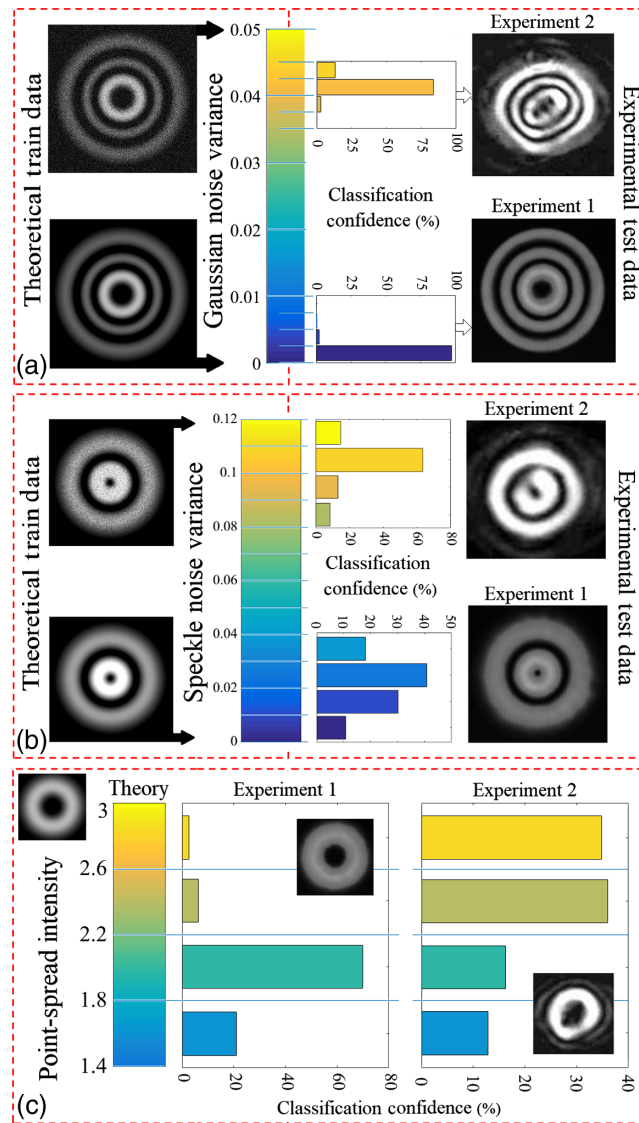


**Fig. 2** Extracting the standard deviation of (a) Gaussian noise and (b) speckle noise in the first and second experiments using the CNN models that are trained over the simulated images of an LG mode with a range of standard deviation in each class, and tested using the experimental images of the same LG mode. (c) Estimating the point-spread intensity using the CNN model to incorporate the effect of camera blur in the experiments on the simulated data.

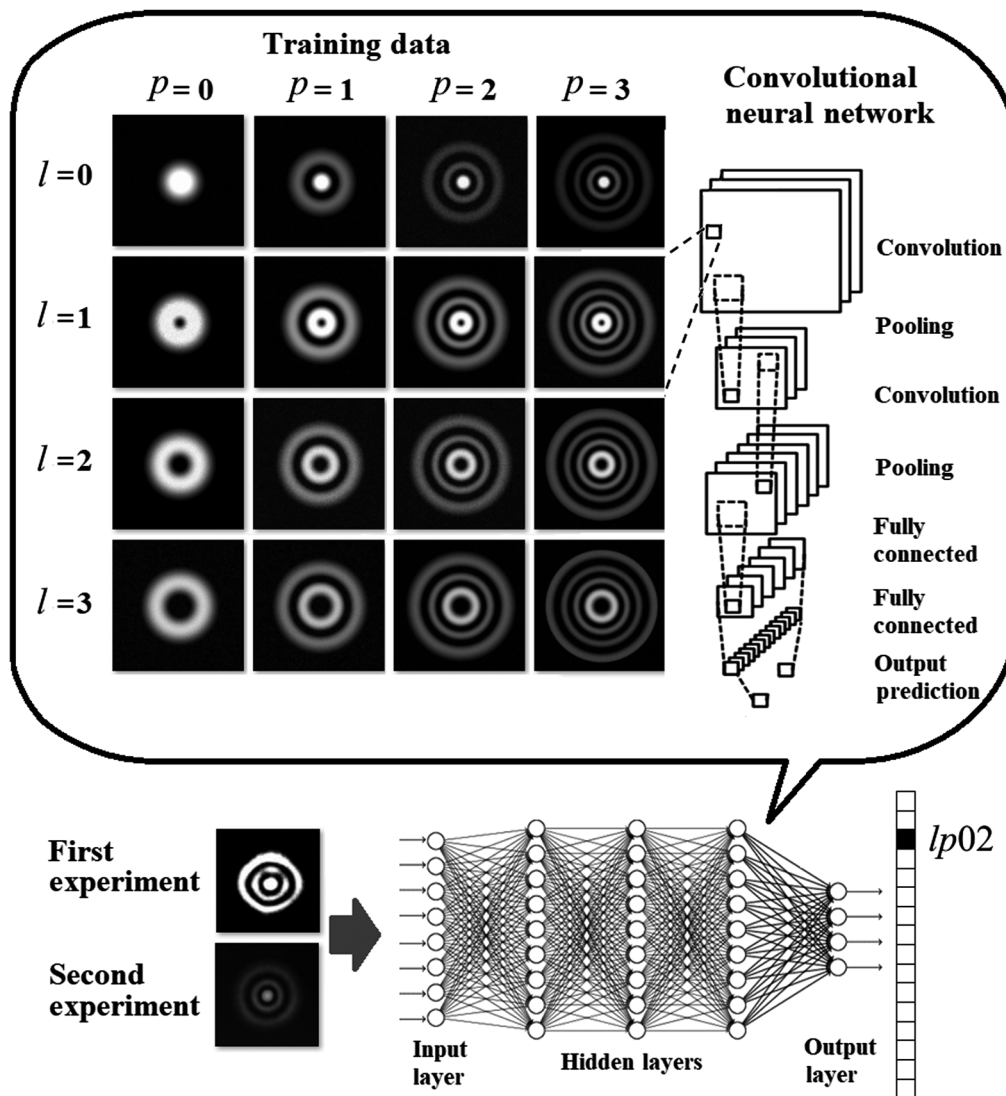
The average signal-to-noise ratios of the LG modes for the first and second experiments are calculated as  $\sim 11$  and  $\sim 3$  dB, respectively. Other significant sources of noise can be the imperfections in the LG modes, such as the discontinuity of the intensity profile and the elliptical nature of the beam. These distortions degrade the accuracy of identifying and classifying the LG modes, especially in the second experiment. The use of experimental test images from two experiments evaluates the performance of CNN models in identifying and classifying the beams with two different degrees of noise in the LG modes and varying nodal structure.

Figure 2(c) shows the CNN model's estimation of the point-spread intensity that is modeled by the *fspecial* function in MATLAB to incorporate the effect of camera blur in the experiments on the simulated data. After the noises and camera blur have been added to the simulated modes, the images are saved in JPEG format ( $600 \times 600$  pixels), and the maximum amplitude and contrast of the simulated modes are scaled to the experimental data. A training dataset and a test dataset are generated with 500 and 20 images, respectively, for each of the LG modes, where  $p$  and  $l$  range from 0 to 3.

### 3 Training Convolutional Neural Network-Based Predictive Model

Conventional machine-learning techniques are not fully automated so they need learning effective features and must extract feature vectors from input patterns through a feature extraction algorithm. The procedure requires human intervention in a training procedure that may affect the accuracy of the classification algorithm.

To develop a predictive model for automatically identifying the LG modes, the CNN architecture within a deep learning framework<sup>27</sup> solves the shortcomings of the existing ML approaches. As a particular type of neural network with deep layer architecture, CNN performs multilayer convolution to extract features and combine the features automatically at the same time on a single network. CNN extracts spatial features from low-level layers that are then passed to aggregation layers (convolutional, pooling, etc.) and additional layers of filters for extracting higher-order features (patterns) that are combined at the top layers. Fully connected layers in the output part of the network perform image interpretation and classification, as shown in Fig. 3(a). As feature extraction and classification are simultaneously performed in a neural network,



**Fig. 3** (a) The training dataset of the first 16 LG modes ( $l$  and  $p$  vary from 0 to 3) is passed to the CNN model that extracts spatial features using aggregation layers (averaging, pooling, etc.), and additional filter layers that are eventually combined at the top layer to predict and classify the new image of the LG mode. (b) Evaluation of the learned network using the random test images of LG modes from the first and second experiments.

features fit for the classification are automatically carried out and further improve performance. Figure 3(b) shows the evaluation of the learning network using the random test images of LG modes from the first and second experiments.

The patches of labeled datasets of the simulated LG modes that were generated for training CNNs are fed into a deep CNN that includes three convolutional layers, three pooling layers, two dropout layers, and two fully connected layers. The size of the training data is optimized for the composition of hidden layers to reach the optimal overall classification performance. The composition of hidden layers relates to the number of convolution and pooling layers, the number of nodes in a convolution layer, and the kernel size of the pooling and convolution masks. The size of each training image and the number of training images determine the optimal number of layers in the CNN. The size of training images and the number of classes affect the mask of layers and the number of nodes, respectively. The performance and reliability of CNN are directly associated with the depth of layers in the neural network and the number of training samples with new information that mimics the experimental imperfections. For a limited number of sample images, increasing the depth of the network is not beneficial as such an approach may result in overfitting that further lowers the reliability of the model. The increase in the image quality (i.e., image pixels) allows expanding the depth of the neural network by adding more layers, possibly improving the CNN performance. However, more layers lead to an exponential increase in the computing cost, which makes necessary the effective parallelization of the repetitive convolution-pooling structure to reduce the computing time.

A rectified linear unit (ReLU) nonlinear activation function is used for the input layer and hidden layers, while a logistic regression (softmax) function is implemented to generate a normalized exponential distribution for the final layer to obtain the final learning probability and predicted labels.<sup>39</sup> A deep CNN has many hidden layers. To learn all the weights in the layers, the loss function is minimized by the batch gradient descent algorithm that is generally used to train a neural network to propagate an error by the chain rule. During the training steps, CNN learns the optimal weights of all layers using forward- and backward-propagation through the neural network architecture. The CNN architecture is employed by retraining a pretrained model, the Inception-v3,<sup>39</sup> in the TensorFlow platform,<sup>46</sup> which was introduced as a deep learning open-source software by Google to identify and classify images. Transfer learning extracts existing knowledge learned from one environment to solve new problems. The pretrained CNN takes advantage of training with a lower amount of data for the new problem and significantly shortens the training procedure. In addition, the predictive model uses the zero-shot learning approach, as the model needs to learn how to recognize new categories of instances by providing a high-level description of the new categories that relate them to categories previously learned by the machine. Here, the zero-shot learning approach is used to recognize the experimental images of LG models with noise and imperfections, even though the training datasets have no experimental images, and the semantic information about the LG modes is provided using simulated data with artificially added noise in the experiments.

In order to test and optimize the performance of the deep CNN model, we conduct systematic convergence studies concerning the iterations, learning rate, and batch size. The learning rate is the most critical hyperparameter for the neural network and affects how quickly our predictive model can converge to the best accuracy. The training and validation accuracies of the predictive model versus the number of iterations for two different learning rates are shown in Fig. 4. The training and test accuracies increase by increasing the number of iterations, and higher learning rates (i.e.,  $\alpha = 0.1$ ) accelerate the convergence of the deep CNN model to higher training and validation accuracies. While choosing this learning rate increases the accuracy more quickly, a larger learning rate makes the optimization process unable to settle in the global minimum of the loss function, lowering the model accuracy. In addition, the fluctuations of the training and validation convergence decrease after  $\sim 100$  iterations at the larger learning rate. This demonstrates that the size of the datasets and the deep CNN model are properly selected, and the model is not suffering from overfitting. Batch size is another important hyperparameter to tune in modern deep learning systems. Choosing a small batch size allows the model to start learning before having to see all the data. However, the model may not converge to the global optima, resulting in a smaller accuracy. As shown in Fig. 4, decreasing the batch size to 8 decreases the accuracy of the predictive model, and the model starts to bounce around the global optimum [Fig. 4(d)].

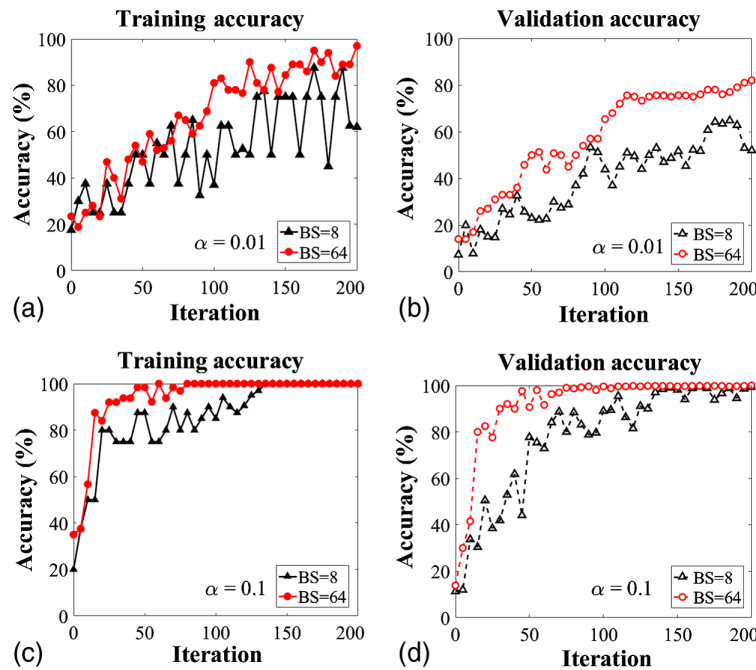


**Fig. 4** Training and test accuracies of the deep CNN predictive model versus the number of iterations for two different learning rates of 0.01 and 0.1 and batch sizes of 8 and 64.

Increasing the batch size cannot lead to further improvement in the model accuracy or computational speedups in nonparallel computer systems. In many cases, depending on the size of training databases, increasing the batch size decreases the model generalization, resulting in lower model accuracy.

## 4 Results

Figure 5 shows the confusion matrix that guides humans to observe the dominant confusing classes of the 16 LG modes [see Fig. 3(a)]. The predicted number of observations classified by the CNN model is shown for 20 test images of the first and second experiments in upper and lower triangles, respectively. The diagonal represents the correctly predicted number of each observation, while off diagonals provide information about the misclassification. For instance, the confusion matrix indicates that the classification model has difficulty in correctly predicting the neighbor classes with the same  $p$  values. It can be noticed that the classification model is more confused in classifying the images of LG modes from the second experiment compared to the first experiment because these images generally have more imperfections and are thus disjointed from the training sets consisting of the simulated LG modes. The model demonstrates the same performance and correctly predicts all the test images of the LG mode  $l = 0, p = 0$  for both experiments.

Two transforms were used during the training process to examine the zero-shot learning approach and CNN's ability to generalize to new data. In the first transform, the training data are only selected from the theory dataset (zero-shot learning), whereas the second transform includes both theory and experimental datasets to increase the diversity of CNN's training data for the classification problem. Figure 6 shows the prediction confidence of the CNN model on two LG modes as examples of true and false predictions for the first experimental set up. For the CNN model that followed the zero-shot learning approach (trained using the simulated modes to test on experimental modes, as shown in dark red and dark blue bars), the LG mode of  $l = 1, p = 3$  is correctly predicted in Fig. 6(a) with about a 5% margin. However, the LG mode of  $l = 1, p = 1$  is incorrectly predicted as  $l = 1, p = 2$  in Fig. 6(b). These prediction confidences are increased to 97% and 99% for the LG modes of  $l = 1, p = 3$  and  $l = 1, p = 1$ , respectively, when the CNN models are trained using both simulated and experimental data (non-zero-shot

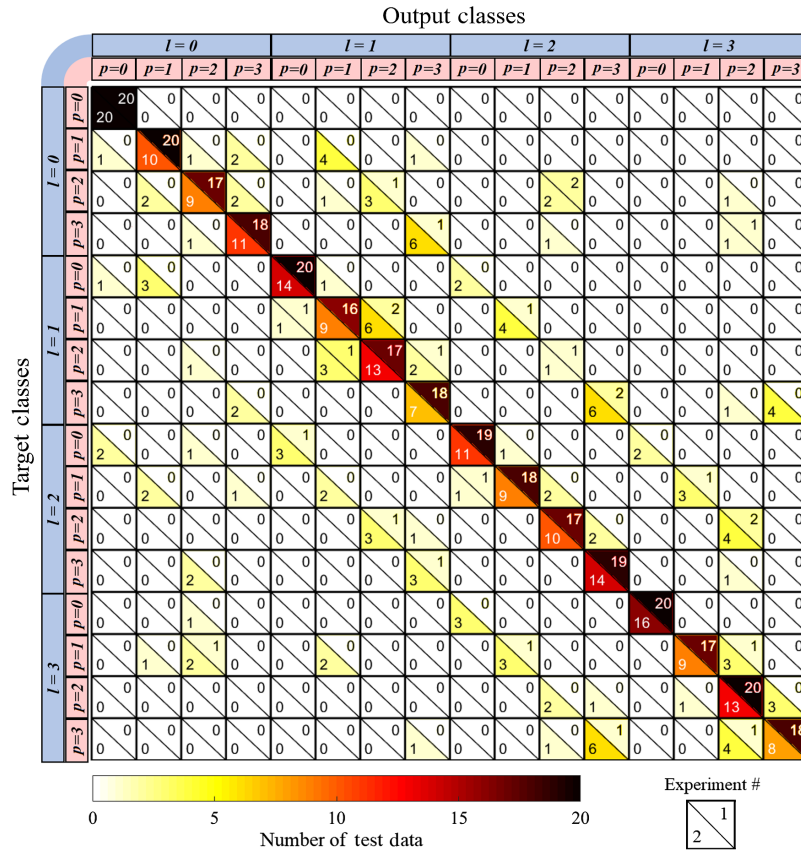


**Fig. 5** Confusion matrix showing the exact number of correctly classified and misclassified images in classifying 16 categories of LG modes.

learning). Similarly, Fig. 6 shows the prediction confidence of two LG modes as examples of true and false predictions for the second experimental set up. For the CNN model that is trained using the simulated images and tested on experimental data [dark red and dark blue in Fig. 6(c)], the LG mode of  $l=0, p=1$  is correctly predicted with a confidence of 88% and margin of  $\sim 85\%$  from the second and third possible modes ( $l=0, p=2$ ). In Fig. 6(d), however, the LG mode of  $l=3, p=1$  is incorrectly predicted as  $l=3, p=2$  with a prediction confidence of 38%. The performance of the zero-learning approach degrades in classifying the neighbor LG modes with the same  $p$  values, as also indicated in the confusion matrix. The CNN model that was trained using both the simulated and experimental data predicted all the LG modes correctly with a confidence larger than 98%. Our results show that increasing the number of layers cannot improve the accuracy of the CNN model in the first transform. To improve the accuracy, more diversified training data of the theoretical images have to be added by incorporating other experimental imperfections, such as intensity discontinuities and distortion in mode shape.

In order to evaluate the ability of the predictive model to identify the LG modes and study its classification performance, five metrics are calculated as follows:

$$\text{Precision} = \text{TP}/(\text{TP} + \text{FP})$$

$$\text{Sensitivity} = \text{TP}/(\text{TP} + \text{FN})$$

$$\text{Specificity} = \text{TN}/(\text{FP} + \text{TN})$$

$$\text{F-score} = 2 \times \text{TP}/(2 \times \text{TP} + \text{FP} + \text{FN})$$

$$\text{Accuracy} = (\text{TP} + \text{TN})/(\text{TP} + \text{FP} + \text{FN} + \text{TN}), \quad (2)$$

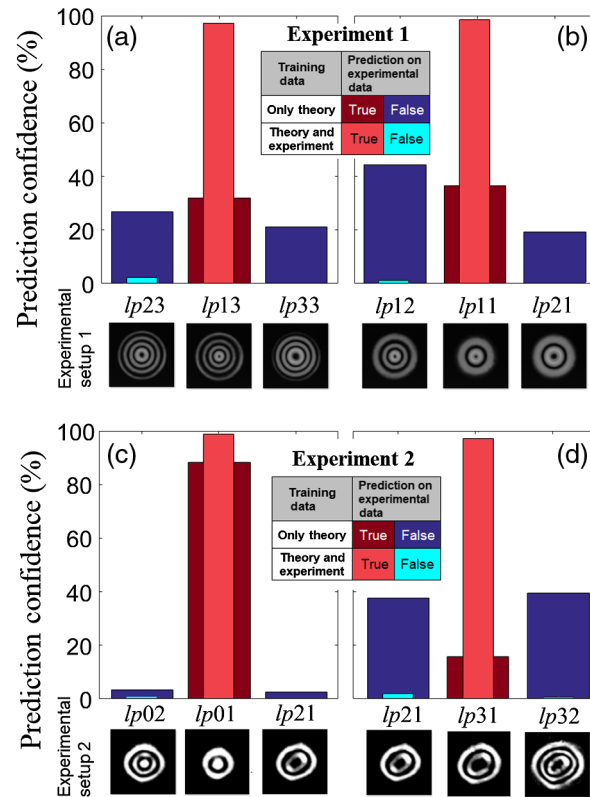


**Fig. 6** Prediction confidence on two LG modes from the first experimental set up for (a)  $l = 1$ ,  $p = 3$  and (b)  $l = 1$ ,  $p = 1$  as examples of true and false predictions, respectively. The dark red and dark blue indicate the results of the CNN models trained using the simulated images, while the light red and light blue indicate the results of the CNN models trained using both the simulated and experimental images. Prediction confidence on two LG modes from the second experimental set up for (c)  $l = 0$ ,  $p = 1$  and (d)  $l = 3$ ,  $p = 1$  as examples of true and false predictions, respectively. The dark red and dark blue indicate the results of the CNN models trained using the simulated images, while the light red and light blue indicate the results of the CNN models trained using both the simulated and experimental images.

where TP, TN, FP, and FN are the true positive, true negative, false positive, and false negative numbers of the LG modes being classified for each class, respectively. The precision can be viewed as a measure of a classifier's exactness, and the sensitivity (or recall) as a measure of a classifier's completeness. Low precision and sensitivity indicate many false positives and many false negatives, respectively. The specificity measures the proportion of correctly identified negatives. The  $F$ -score considers both precision and recall. The  $F$ -score becoming 0 indicates the worst accuracy, while the best accuracy corresponds to 1.

Figure 7 shows five measures that are computed for the performance analysis of the predictive classification model for each LG mode and two experimental setups. It can be noticed from Fig. 7(a) that the accuracies of all 16 classes of LG modes are above 97% and 90% for the first and second experiments, respectively. The accuracy refers to the true predictions among the total validation. The classification model has a worse performance in classifying the LG modes from the second experiment compared to the first experiment because they are more disjointed from the training sets consisting of the simulated LG modes. For the LG mode  $l = 0$ ,  $p = 0$  whose profile is a simple filled circle, the accuracy of predictive models reaches the maximum values of 100% and 98.7% for the first and second experiments, respectively. The model demonstrates the same performance in the confusion matrix and correctly predicts all test images. However, the model falsely misclassifies four additional LG modes to this LG mode (false positive). This degrades the maximum accuracy (classifier's exactness) for the second experiment. Similarly, the specificity measures [Fig. 7(b)] of all 16 classes of LG modes are

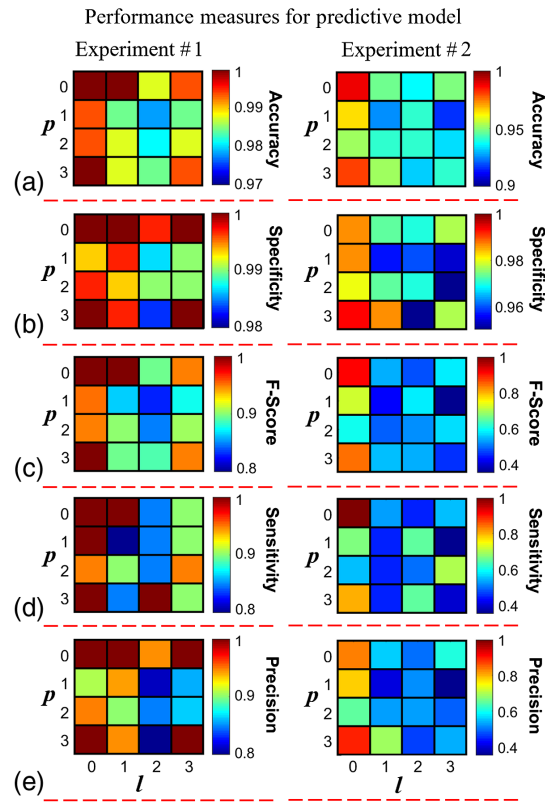


**Fig. 7** Analysis of five statistical metrics: (a) accuracy, (b) specificity, (c)  $F$ -score, (d) sensitivity, and (e) precision for the model prediction in assigning the test images of the first and second experiments to 16 classes of LG modes trained by the simulated data and tested by the experimental data.

above 98% and 95% for the first and second experiments, respectively, demonstrating the classifier's completeness and exceeding the performance of conventional conjugate methods.<sup>21</sup>

In addition to high accuracy or high specificity, however, a sound classifier must also demonstrate high performance for the other measures. In Figs. 7(c)–7(e), the  $F$ -score, sensitivity, and precision of the predictive model for the two experiments are shown. It can be noticed that the  $F$ -score of the second experiment can be as low as 35% with an average of 57%, demonstrating the model prediction of many false positives and many false negatives in classifying the 16 LG modes. However, the minimum  $F$ -score of the first experiment is about 80% with an average of 92% in classifying the 16 LG modes. Similar results can be seen for the sensitivity and precision of the first and second experimental set ups. In summary, considering all five classification measures, the CNN model that is trained using the theory dataset (zero-shot learning) performs well for the first experiment. However, the CNN demonstrates degraded performance in classifying the 16 LG modes for the second experiment due to more noise and the existence of other experimental imperfections such as intensity discontinuities and distortion in mode shape (i.e., deviations from perfect roundedness).

## 5 Discussion

In this paper, we employed a CNN model that reaches accuracies of  $\sim 99\%$  and  $\sim 94\%$  in recognizing LG modes for the first and second experiments, respectively. CNNs outperform other ML models such as  $K$ -nearest neighbor (KNN) algorithms and ANNs, especially under strong turbulence. KNN algorithms have high computational complexity and high sample imbalance, while ANNs require manual extraction of the features of original images.<sup>47</sup> Li et al.<sup>47</sup> demonstrated that CNN-based adaptive demodulators of the OAM shift-keying (OAM-SK) system have lower error rates than KNN-based and ANN-based devices. The developed CNN model

in this paper includes three convolutional layers, three pooling layers, two dropout layers, and two fully connected layers. Larger numbers of CNN layers potentially improve the recognition accuracy.<sup>21</sup> However, a trade-off exists between the efficiency of recognition and the complexity of CNN models. Multihidden layer networks require longer computation time, more training parameters, and a more sophisticated training algorithm that cannot be handled by the central processing unit. They require a graphics processing unit that is capable of handling large-scale parallel computing. In addition, in the case of zero-shot learning in which the CNN observes OAM from classes that were not observed during training, the lower accuracy could be attributed to the lack of sufficient similar and diversified training data. Following the zero-shot learning approach, further improvement could be possibly achieved by diversifying the training data of the theoretical images through incorporating other experimental imperfections, such as intensity discontinuities and distortion in the modal shape. Figure 6 shows that incorporating both theoretical and experimental datasets to increase the diversity of CNN's training data about the classification problem leads to 100% correct prediction of the modes (with confidence larger than 98%) for the second transform with the same number of layers in the neural network. In addition, the choice of OAM modes and mode spacing for the training data of the CNN model can also impact its final accuracy, since the intensity pattern of some modes is less sensitive to noise such as turbulence, so that the classification of these modes by the CNN is relatively simpler. For instance, symmetrical OAM modes with the same absolute value but opposite signs can be multiplexed to form petal-like intensity patterns that are less sensitive to the effects of turbulence.<sup>32,47–49</sup>

The developed CNN model can also be employed for other types of OAM carrying beams such as vortex beams (VBs)<sup>50–55</sup> in which the azimuthal phase dependence of OAM is coupled with a helicoidal transverse polarization pattern. Decoding the information stored in VBs is highly desirable for applications such as quantum information processing.<sup>56,57</sup> However, the use of conventional approaches to decode the information stored in VBs is challenging because they require interferometry<sup>58,59</sup> or spatial filtering.<sup>60,61</sup> The effects of loss and noise<sup>62</sup> on the state tomography make these techniques unreliable for characterization and classification of VBs.<sup>50</sup> For instance, the interferometric methods are susceptible to collimation accuracy and environmental perturbations, because slight misalignment or vibrations destroy the interference patterns and decrease the identification accuracy. In addition, interferometry and diffraction methods have low speed and limited information extraction capability.<sup>63</sup> For instance, Fickler et al.<sup>64</sup> showed that sorting the radial index of LG modes is possible using a random scattering process that reshapes the phase structure of the incident light. However, this approach has low efficiency due to the strong multimode nature of the scattering process. Similarly, a mode sorter was designed<sup>65</sup> based on the fractional Fourier transform that decomposes the optical field and thereby separates individual radial modes that were indexed by the value of their radial quantum number. This approach has also low efficiency due to its complexity.

In this paper, we used CNN models for LG modes that can be similarly employed to extract the OAM mode signal from distorted VBs. ML methods have significant advantages for recognizing and classifying specific polarization patterns of VBs,<sup>66</sup> resulting in the accurate construction and characterization<sup>50</sup> of high-dimensional resources for quantum protocols. ML can recognize unconjugated OAM modes<sup>1,47,66</sup> in which the feature parameters are created by interfering the VB with its mirror image in interferometry. To identify conjugated OAM modes, new designs such as two-dimensional fork gratings<sup>63</sup> can be used to produce diffraction patterns of VBs with different feature parameters for training ML models. The CNN-based OAM recognition system provides a promising approach to efficiently recognize and extract the properties of high-dimensional photonic VB systems.<sup>50</sup> CNNs eliminate the need for additional interferometry stabilization and spatial filtering in decoding information stored in VBs and thereby provide a robust technique to manage higher-dimensional quantum systems.<sup>67</sup> Bekerman et al.<sup>68</sup> used neural networks to develop a general framework of the optical mode sorter based on both the OAM value<sup>69,70</sup> and the radial index,<sup>65,71</sup> demonstrating that ML can be used to distinguish between OAM beams. More specifically, different beams that possess OAM can be distinguished without interferometry according to a different set of radial quantum numbers that correspond to the effective phase velocity as a key property of the VB modes. However, further studies are required to examine ML's ability to classify other types of OAM beams, such as beams with a Gaussian

intensity profile before the beam propagates.<sup>52,53</sup> In general, the CNN-based OAM recognition system promotes the application of VBs in classical and quantum optics,<sup>72</sup> including optical microscopy and imaging,<sup>73,74</sup> quantum information,<sup>75</sup> optical storage,<sup>76</sup> particle trapping,<sup>74</sup> and free-space communications.<sup>75</sup>

Generating, transmitting, and sorting states of light with different OAM values greatly increase the transfer rate of free-space optical communications to the Tb/s range.<sup>3,22,77</sup> To produce the constant frequency and spatial mode<sup>78</sup> for this application, the temperature, current, and grating position of the laser must be carefully tuned. However, under some external influence in optical experiments, mode hops can make a laser simultaneously oscillate in many modes, making the correct detection of the actual OAM mode challenging. The CNN-based OAM recognition model is promising for self-tuning of the laser through feedback to improve the instability in the laser output or subsequent beam delivery optics. CNNs contain the relevant feature extraction that can be used to enable self-tuning mode-locked lasers (MLL).<sup>79</sup> CNN-based recognition of beam translation and rotation can improve the performance of MLL fabrication resulting in higher precision and reproducibility. CNNs have the capability of detecting multiple laser machining parameters from the camera simultaneously that can be used to adjust the laser parameters (e.g., laser power) concurrently.<sup>80</sup> Xie et al.<sup>81</sup> developed a real-time closed-loop feedback system, demonstrating that CNNs are efficient for detecting unintentional laser beam translations and rotations<sup>82</sup> and identifying laser machining parameters simultaneously. CNN-based OAM recognition techniques can be used to optimize experiments because CNNs can be trained by experimental data without requiring understanding of the physical properties of the laser. ML techniques prove to be useful for many experimental tasks related to structured light in quantum technologies, especially for detecting and demultiplexing OAM in the context of classical and quantum communications. Demultiplexing of two modes has been experimentally demonstrated<sup>68</sup> and the number of modes could be extended to 12.<sup>83</sup>

The CNN-based OAM recognition model has a promising application for the OAM-SK system in free-space optical communications in which the system requires rapid encoding of OAM modes to digital signals. Currently, the benefit of OAM-SK is limited due to the lack of effective detection methods to adapt the rapidly switched modes. ML techniques can be used for high-speed and accurate detection of OAM modes. He et al.<sup>63</sup> demonstrated that the OAM modes of VBs ranging from  $-25$  to  $+25$  could be quickly identified, and that the classification accuracy reaches 99.55% after training with images influenced by the propagation distance, beam waist, and atmospheric turbulence. Krenn et al.<sup>32</sup> used an ANN to distinguish between the transmitted OAM modes of light that have significant distortion after propagation over a distance of 143 km. The algorithm reaches an accuracy of more than 80% and decodes the transmitted message with an error rate of 8.33%. Similarly, Li et al.<sup>47</sup> demonstrated that CNNs consisting of five-layers (two convolution layers, two pooling layers, and one fully connected layer) can detect 16-ary OAM with a recognition accuracy of  $\sim 84\%$  after propagating over 2 km under strong turbulence.

Conventional mode recognition techniques such as the correlation filter method (CFM)<sup>84</sup> reach a mode detection rate up to 30 Hz by utilizing a set of transmission functions encoded in a computer-generated hologram.<sup>85</sup> While the speed of CFM depends on the alignment and calibration of the optical systems, methods based on the CNN model only need a CCD camera to capture the beam intensity profile and recognize the optical modes. Although the spatially and spectrally (S2) resolved method<sup>86</sup> requires no prior detailed knowledge of the optical systems, this technique requires longer measurement time and is thus unsuitable for real-time modal recognition. Other methods such as the stochastic parallel gradient descent algorithm include an iterative search process that limits the rate of mode recognition to 9 Hz.<sup>87</sup> OAM mode sorting based on unitary transformations<sup>88</sup> can convert the azimuthal phase profile of an OAM mode to a set of truncated plane waves and then separate them by a single lens. While in theory a power transmission efficiency of unity can be achieved, the diffraction due to the finite size of the unwrapped modes limits the degree of separation of two adjunct OAM modes, diminishing the efficiency of this mode sorting approach.<sup>89</sup>

Deep neural networks have been used for many tasks of real-time image recognition, including autonomous driving,<sup>90</sup> facial expression,<sup>91</sup> texture synthesis,<sup>92</sup> medical imaging,<sup>93</sup> and optical communications.<sup>94</sup> An et al.<sup>95</sup> used CNNs for real-time mode decomposition to identify

the intrinsic mode properties of multimode fibers. The decomposition rate of CNNs can reach  $\sim 200$  Hz when testing on the simulated beam profiles and  $\sim 30$  Hz when testing on the experimental beam profiles due to the restriction imposed by the maximum frame rate of the CCD camera.<sup>95</sup> The real-time mode recognition and decomposition capability of deep CNNs can be improved using a camera with a higher frame rate.

## 6 Conclusions

Theoretical simulations coupled with measured experimental data and assisted by ML are beginning to play an integral role in automated analysis and adaptive control of optical experiments. In this paper, we apply an ML model to automatically detect and classify the LG modes. This research will enable the full potential and applications of OAM of light by developing improved sensing and imaging technologies. We train CNNs with the zero-shot learning approach by generating the experimental and simulated datasets of the lowest 16 LG modes that rely only on the intensity images of their unique patterns. The predictive model is optimized to reach high overall classification performance by conducting systematic convergence studies with respect to the epochs, learning rate, and batch size. The experimental test data are generated using two experimental set ups with different noise intensity, spatial dislocation, and nonuniform intensity in LG modes in order to examine the performance of the CNN model under different experimental conditions. Five performance measures of the predictive classification model are computed for each LG mode. The model demonstrates both accuracy and specificity above 90% in classifying the 16 LG modes for both experimental set ups. The  $F$ -score, sensitivity, and precision of the second experiment are 35% for some LG modes with an average of 57%, due to larger experimental imperfections such as intensity discontinuities and distortion in mode shape. However, those of the first experiment are above 80% with an average of 92%. In conclusion, the CNN model that is trained using the theory dataset (zero-shot learning) performs well for the first experiment, while its performance in classifying the LG modes decreases for the second experiment.

## Acknowledgments

This work was completed shortly after the tragic death of our colleague, Professor Jonathan P. Dowling. It is with immense gratitude that we acknowledge his close friendship, his guidance, and his insight, which we sorely miss. We would like to thank Ms. Savannah Cuzzo, Mr. Narayan Bhusal, Dr. Irina Novikova, and Dr. Omar Magana-Loaiza for valuable discussions and help in collecting the experimental data.

## References

1. S. Lohani et al., “On the use of deep neural networks in optical communications,” *Appl. Opt.* **57**(15), 4180–4190 (2018).
2. A. M. Yao and M. J. Padgett, “Orbital angular momentum: origins, behavior and applications,” *Adv. Opt. Photonics* **3**(2), 161–204 (2011).
3. G. Gibson et al., “Free-space information transfer using light beams carrying orbital angular momentum,” *Opt. Express* **12**(22), 5448–5456 (2004).
4. D. R. Elgort and L. R. Albu, “Magnetic resonance imaging hyperpolarization of liquids or solids by light with orbital angular momentum,” Google Patents US8765099B2 (2014).
5. N. Uribe-Patarroyo et al., “Detecting photons with orbital angular momentum in extended astronomical objects: application to solar observations,” *Astron. Astrophys.* **526**, A56 (2011).
6. Z. Sheng-Mei et al., “A large-alphabet quantum key distribution protocol using orbital angular momentum entanglement,” *Chin. Phys. Lett.* **30**(6), 060305 (2013).
7. D. S. Simon, *A Guided Tour of Light Beams*, Morgan & Claypool Publishers, San Rafael, California (2016).
8. M. Clifford et al., “High-order Laguerre–Gaussian laser modes for studies of cold atoms,” *Opt. Commun.* **156**(4-6), 300–306 (1998).

9. L. Hofer et al., “Hermite–Gaussian mode detection via convolution neural networks,” *JOSA A* **36**(6), 936–943 (2019).
10. F. Gori, G. Guattari, and C. Padovani, “Bessel-Gauss beams,” *Opt. Commun.* **64**(6), 491–495 (1987).
11. J. C. Gutiérrez-Vega, M. Iturbe-Castillo, and S. Chávez-Cerda, “Alternative formulation for invariant optical fields: Mathieu beams,” *Opt. Lett.* **25**(20), 1493–1495 (2000).
12. M. A. Bandres and J. C. Gutiérrez-Vega, “Ince–Gaussian beams,” *Opt. Lett.* **29**(2), 144–146 (2004).
13. M. A. Cox et al., “The resilience of Hermite– and Laguerre–Gaussian modes in turbulence,” *J. Lightwave Technol.* **37**(16), 3911–3917 (2019).
14. L. Allen et al., “Orbital angular momentum of light and the transformation of Laguerre–Gaussian laser modes,” *Phys. Rev. A* **45**(11), 8185 (1992).
15. A. Mair et al., “Entanglement of the orbital angular momentum states of photons,” *Nature* **412**(6844), 313–316 (2001).
16. H. He et al., “Direct observation of transfer of angular momentum to absorptive particles from a laser beam with a phase singularity,” *Phys. Rev. Lett.* **75**(5), 826 (1995).
17. S. Franke-Arnold, “Optical angular momentum and atoms,” *Philos. Trans. R. Soc. A: Math. Phys. Eng. Sci.* **375**(2087), 20150435 (2017).
18. B. Ndagano et al., “Comparing mode-crosstalk and mode-dependent loss of laterally displaced orbital angular momentum and Hermite–Gaussian modes for free-space optical communication,” *Opt. Lett.* **42**(20), 4175–4178 (2017).
19. M. Li, “Orbital-angular-momentum multiplexing optical wireless communications with adaptive modes adjustment in internet-of-things networks,” *IEEE Internet Things J.* **6**(4), 6134–6139 (2018).
20. M. Li, Z. Yu, and M. Cvijetic, “Influence of atmospheric turbulence on OAM-based FSO system with use of realistic link model,” *Opt. Commun.* **364**, 50–54 (2016).
21. T. Doster and A. T. Watnik, “Machine learning approach to OAM beam demultiplexing via convolutional neural networks,” *Appl. Opt.* **56**(12), 3386–3396 (2017).
22. J. Wang et al., “Terabit free-space data transmission employing orbital angular momentum multiplexing,” *Nat. Photonics* **6**(7), 488 (2012).
23. Y. Ren et al., “Atmospheric turbulence effects on the performance of a free space optical link employing orbital angular momentum multiplexing,” *Opt. Lett.* **38**(20), 4062–4065 (2013).
24. L. R. Hofer, R. V. Dragone, and A. D. MacGregor, “Scale factor correction for Gaussian beam truncation in second moment beam radius measurements,” *Opt. Eng.* **56**(4), 043110 (2017).
25. Y. Banadaki and S. Sharifi, “Cyber-enabled distributed machine learning for smart manufacturing systems,” *Proc. SPIE* **10973**, 109730Z (2019).
26. S. Sharifi, “Applications of stochastic optimization and machine learning in photonic nanostructures and quantum optical systems,” Doctoral Dissertation (2020).
27. S. Hoo-Chang et al., “Deep convolutional neural networks for computer-aided detection: CNN architectures, dataset characteristics and transfer learning,” *IEEE Trans. Med. Imaging* **35**(5), 1285 (2016).
28. A. Quattoni, M. Collins, and T. Darrell, “Transfer learning for image classification with sparse prototype representations,” in *IEEE Conf. Comput. Vision and Pattern Recognit., CVPR 2008*, pp. 1–8 (2008).
29. Y. Taigman et al., “Deepface: closing the gap to human-level performance in face verification,” in *Proc. IEEE Conf. Comput. Vision and Pattern Recognit.*, pp. 1701–1708 (2014).
30. N. Razaviarab, S. Sharifi, and Y. M. Banadaki, “Smart additive manufacturing empowered by a closed-loop machine learning algorithm,” *Proc. SPIE* **10969**, 109690H (2019).
31. S. Sharifi et al., “Identifying Laguerre–Gaussian modes using convolutional neural network,” in *IEEE 18th Int. Conf. Mach. Learn. and Appl.*, pp. 924–927 (2019).
32. M. Krenn et al., “Twisted light transmission over 143 km,” *Proc. Natl. Acad. Sci. U. S. A.* **113**(48), 13648–13653 (2016).
33. P. Wang et al., “Convolutional neural network-assisted optical orbital angular momentum recognition and communication,” *IEEE Access* **7**, 162025–162035 (2019).

34. Z. Wang et al., “Efficient recognition of the propagated orbital angular momentum modes in turbulences with the convolutional neural network,” *IEEE Photonics J.* **11**(3), 1–14 (2019).
35. M. E. Anderson et al., “Measuring the topological charge of ultrabroadband, optical-vortex beams with a triangular aperture,” *JOSA B* **29**(8), 1968–1976 (2012).
36. C.-S. Guo, L.-L. Lu, and H.-T. Wang, “Characterizing topological charge of optical vortices by using an annular aperture,” *Opt. Lett.* **34**(23), 3686–3688 (2009).
37. V. Denisenko et al., “Determination of topological charges of polychromatic optical vortices,” *Opt. Express* **17**(26), 23374–23379 (2009).
38. M. Padgett and L. Allen, “Orbital angular momentum exchange in cylindrical-lens mode converters,” *J. Opt. B: Quantum Semiclass. Opt.* **4**(2), S17 (2002).
39. C. Szegedy et al., “Rethinking the inception architecture for computer vision,” in *Proc. IEEE Conf. Comput. Vision and Pattern Recognit.*, pp. 2818–2826 (2016).
40. S. Sharifi et al., “Improving the measurement of squeezed states using noise subtraction techniques,” *Bull. Am. Phys. Soc.* (2020).
41. S. L. Cuozzo et al., “Improving quantum noise suppression using spatial beam profile optimization,” in *Laser Sci.*, p. JT4A.3 (2019).
42. E. Hemsing et al., “Coherent optical vortices from relativistic electron beams,” *Nat. Phys.* **9**(9), 549–553 (2013).
43. Y. Li, J. Kim, and M. J. Escuti, “Orbital angular momentum generation and mode transformation with high efficiency using forked polarization gratings,” *Appl. Opt.* **51**(34), 8236–8245 (2012).
44. A. E. Siegman, *Lasers*, University Science Books, Mill Valley, California (1986).
45. O. Hirota and J. Toda, “Theory of multiplicative noise caused by coupling loss and amplitude vector rotation in optical communication channels,” *IEEE Trans. Commun.* **31**(8), 992–999 (1983).
46. M. Abadi et al., “Tensorflow: a system for large-scale machine learning,” in *OSDI*, pp. 265–283 (2016).
47. J. Li, M. Zhang, and D. Wang, “Adaptive demodulator using machine learning for orbital angular momentum shift keying,” *IEEE Photonics Technol. Lett.* **29**(17), 1455–1458 (2017).
48. M. Krenn et al., “Communication with spatially modulated light through turbulent air across Vienna,” *New J. Phys.* **16**(11), 113028 (2014).
49. E. Knutson et al., “Deep learning as a tool to distinguish between high orbital angular momentum optical modes,” *Proc. SPIE* **9970**, 997013 (2016).
50. M. Padgett, J. Courtial, and L. Allen, “Light’s orbital angular momentum,” *Phys. Today* **57**(5), 35–40 (2004).
51. M. Erhard et al., “Twisted photons: new quantum perspectives in high dimensions,” *Light: Sci. Appl.* **7**(3), 17146–17146 (2018).
52. T. Giordani et al., “Machine learning-based classification of vector vortex beams,” *Phys. Rev. Lett.* **124**(16), 160401 (2020).
53. Y. S. Rumala, “Propagation of structured light beams after multiple reflections in a spiral phase plate,” *Opt. Eng.* **54**(11), 111306 (2015).
54. G. Vallone et al., “Birth and evolution of an optical vortex,” *Opt. Express* **24**(15), 16390–16395 (2016).
55. Y. S. Rumala and A. E. Leanhardt, “Optical vortex with a small core and Gaussian intensity envelope for light-matter interaction,” *JOSA B* **34**(5), 909–918 (2017).
56. M. Paris and J. Rehacek, *Quantum State Estimation*, Springer Science & Business Media, Berlin, Heidelberg (2004).
57. K. Banaszek, M. Cramer, and D. Gross, “Focus on quantum tomography,” *New J. Phys.* **15**(12), 125020 (2013).
58. J. Leach et al., “Measuring the orbital angular momentum of a single photon,” *Phys. Rev. Lett.* **88**(25), 257901 (2002).
59. T. Bauer et al., “Nanointerferometric amplitude and phase reconstruction of tightly focused vector beams,” *Nat. Photonics* **8**(1), 23–27 (2014).
60. E. Bolduc et al., “Exact solution to simultaneous intensity and phase encryption with a single phase-only hologram,” *Opt. Lett.* **38**(18), 3546–3549 (2013).

61. M. Malik et al., “Direct measurement of a 27-dimensional orbital-angular-momentum state vector,” *Nat. Commun.* **5**, 3115 (2014).
62. H. Qassim et al., “Limitations to the determination of a Laguerre–Gauss spectrum via projective, phase-flattening measurement,” *JOSA B* **31**(6), A20–A23 (2014).
63. Y. He et al., “Detecting orbital angular momentum modes of vortex beams using feed-forward neural network,” *J. Lightwave Technol.* **37**(23), 5848–5855 (2019).
64. R. Fickler, M. Ginoya, and R. W. Boyd, “Custom-tailored spatial mode sorting by controlled random scattering,” *Phys. Rev. B* **95**(16), 161108 (2017).
65. Y. Zhou et al., “Sorting photons by radial quantum number,” *Phys. Rev. Lett.* **119**(26), 263602 (2017).
66. J. Li et al., “Joint atmospheric turbulence detection and adaptive demodulation technique using the CNN for the OAM-FSO communication,” *Opt. Express* **26**(8), 10494–10508 (2018).
67. S. Sharifi et al., “Design of microresonators to minimize thermal noise below the standard quantum limit,” *Rev. Sci. Instrum.* **91**(5), 054504 (2020).
68. A. Bekerman et al., “Beam profiler network (BPNet): a deep learning approach to mode demultiplexing of Laguerre–Gaussian optical beams,” *Opt. Lett.* **44**(15), 3629–3632 (2019).
69. S. Lightman et al., “Miniature wide-spectrum mode sorter for vortex beams produced by 3D laser printing,” *Optica* **4**(6), 605–610 (2017).
70. A. Ruelas, S. Lopez-Aguayo, and J. C. Gutiérrez-Vega, “A Hankel transform distribution algorithm for paraxial wavefields with an application to free-space optical beam propagation,” *J. Opt.* **18**(9), 095605 (2016).
71. X. Gu et al., “Gouy phase radial mode sorter for light: concepts and experiments,” *Phys. Rev. Lett.* **120**(10), 103601 (2018).
72. L. Marrucci et al., “Spin-to-orbital conversion of the angular momentum of light and its classical and quantum applications,” *J. Opt.* **13**(6), 064001 (2011).
73. A. E. Willner et al., “Optical communications using orbital angular momentum beams,” *Adv. Opt. Photonics* **7**(1), 66–106 (2015).
74. F. Cardano and L. Marrucci, “Spin–orbit photonics,” *Nat. Photonics* **9**(12), 776–778 (2015).
75. D. Cozzolino et al., “Air-core fiber distribution of hybrid vector vortex-polarization entangled states,” *Adv. Photonics* **1**(4), 046005 (2019).
76. Z. Dutton and J. Ruostekoski, “Transfer and storage of vortex states in light and matter waves,” *Phys. Rev. Lett.* **93**(19), 193602 (2004).
77. N. Bozinovic et al., “Terabit-scale orbital angular momentum mode division multiplexing in fibers,” *Science* **340**(6140), 1545–1548 (2013).
78. S. Sivaprakasam et al., “Mode hopping in external-cavity diode lasers,” *Opt. Lett.* **21**(6), 411–413 (1996).
79. T. Baumeister, S. L. Brunton, and J. N. Kutz, “Deep learning and model predictive control for self-tuning mode-locked lasers,” *JOSA B* **35**(3), 617–626 (2018).
80. B. Mills et al., “Predictive capabilities for laser machining via a neural network,” *Opt. Express* **26**(13), 17245–17253 (2018).
81. Y. Xie et al., “Deep learning for the monitoring and process control of femtosecond laser machining,” *J. Phys.: Photonics* **1**(3), 035002 (2019).
82. Y. S. Rumala, “Optical vortex rotation and propagation from a spiral phase plate resonator with surface reflective coating,” *Opt. Lett.* **45**(6), 1555–1558 (2020).
83. K. Ingerslev et al., “12 mode, WDM, MIMO-free orbital angular momentum transmission,” *Opt. Express* **26**(16), 20225–20232 (2018).
84. D. Flamm et al., “Mode analysis with a spatial light modulator as a correlation filter,” *Opt. Lett.* **37** (13), 2478–2480 (2012).
85. D. Flamm et al., “Fast M2 measurement for fiber beams based on modal analysis,” *Appl. Opt.* **51** (7), 987–993 (2012).
86. J. Nicholson et al., “Spatially and spectrally resolved imaging of modal content in large-mode-area fibers,” *Opt. Express* **16** (10), 7233–7243 (2008).
87. L. Huang et al., “Real-time mode decomposition for few-mode fiber based on numerical method,” *Opt. Express* **23** (4), 4620–4629 (2015).

88. G. C. Berkhout et al., “Efficient sorting of orbital angular momentum states of light,” *Phys. Rev. Lett.* **105** (15), 153601 (2010).
89. M. Mirhosseini et al., “Efficient separation of the orbital angular momentum eigenstates of light,” *Nat. Commun.* **4** (1), 1–6 (2013).
90. B. Wu et al., “Squeezedet: unified, small, low power fully convolutional neural networks for real-time object detection for autonomous driving,” in *Proc. IEEE Conf. Comput. Vision and Pattern Recognit. Workshops*, pp. 129–137 (2017).
91. I. Song, H.-J. Kim, and P. B. Jeon, “Deep learning for real-time robust facial expression recognition on a smartphone,” in *IEEE Int. Conf. Consum. Electron. (ICCE)*, pp. 564–567 (2014).
92. C. Li and M. Wand, “Precomputed real-time texture synthesis with markovian generative adversarial networks,” in *Eur. Conf. Comput. Vision*, pp. 702–716 (2016).
93. S. S. M. Salehi et al., “Real-time automatic fetal brain extraction in fetal MRI by deep learning,” in *IEEE 15th Int. Symp. Biomed. Imaging (ISBI 2018)*, pp. 720–724, (2018).
94. U. Kürüm et al., “Deep learning enabled real time speckle recognition and hyperspectral imaging using a multimode fiber array,” *Opt. Express* **27**(15), 20965–20979 (2019).
95. Y. An et al., “Deep learning-based real-time mode decomposition for multimode fibers,” *IEEE J. Sel. Top. Quantum Electron.* **26**(4), 1–6 (2020).

**Safura Sharifi** received her PhD in electrical engineering from Louisiana State University, Baton Rouge, Louisiana, in 2020. She also received two master’s degrees in electrical engineering and natural science in 2017 and 2018, respectively, and a graduate certification in material science in 2019, all from LSU. Her research interests include the application of computational analysis, stochastic optimization, and machine learning modeling in nanophotonics and quantum optics.

**Yaser Banadaki** received his PhD in electrical and computer engineering from Louisiana State University, Baton Rouge, Louisiana, in 2016. He is currently an assistant professor with the Department of Computer Science, Southern University, Baton Rouge, Louisiana. His current research focuses on machine learning-based knowledge discovery in science and engineering, including electronic and photonic nanostructures, material science, quantum optics, cybersecurity, and quantum computers.

**Georgios Veronis** received his PhD in electrical engineering from Stanford University in 2002. He is currently a professor with the School of Electrical Engineering and Computer Science, Louisiana State University, Baton Rouge, Louisiana. His current research focuses on the theory and simulation of photonic materials, nanoscale photonic devices, plasmonics, and computational electromagnetics.

**Jonathan P. Dowling** received his PhD in mathematical physics from the University of Colorado at Boulder in 1988. He was a professor with the Department of Physics and Astronomy, Louisiana State University. He was an expert in the field of quantum science and technologies, including quantum electrodynamics, quantum optics, quantum information theory, and photonic band-gap materials.